Studies of Gas Flow Impedance in the LUX-ZEPLIN Radon Removal System

by

Michael Reh

A dissertation submitted in partial fulfillment
of the requirements for the degree of
Bachelor of Science
(Honors Physics)
at The University of Michigan
2019

Undergraduate Advisor:

Professor Wolfgang Lorenzon

ACKNOWLEDGEMENTS

I would like to thank Professor Wolfgang Lorenzon for providing me with the opportunity to take on this research project and encouraging me through to its completion. I would also like to thank Maris Arthurs and Priyashree Roy for helping to assemble the system and conduct measurements; this certainly would have been much more difficult without their help and guidance. Additionally, I would like to thank Dr. Richard Raymond for providing me with insight and resources not only in the experimental phase, but in the analysis as well. Finally, I'd like to thank my thesis writing support group (Mariam, Camille, and Sonalee) for providing feedback on my writing along the way, and for forcing me to write even on days I wasn't feeling up to it.

TABLE OF CONTENTS

LIST OF FIGURES

Figure

LIST OF TABLES

Table

LIST OF ABBREVIATIONS

LZ LUX-ZEPLIN

RRS Radon Removal System

slpm standard liters per minute

WIMP Weakly Interacting Massive Particle

XPS Xenon Purification System

ABSTRACT

Studies of Gas Flow Impedance in the LUX-ZEPLIN Radon Removal System
by
Michael Reh

Advisor: Professor Wolfgang Lorenzon

Studies of gas flow dynamics of argon and nitrogen gases through the LUX-ZEPLIN (LZ) Radon Removal System assembled at half strength will be discussed. Flow impedance measurements were conducted at 0.5, 1.0, and 2.0 standard liters per minute through Saratech charcoal. Tests were performed at 295 K and 188 K, at 1 bar and 1.6 bar, and using different combinations of the LZ Radon Removal System traps. It was found that in general, the flow impedance introduced by the traps increases with increasing flow rate, decreases with increasing pressure, decreases with decreasing temperature, is higher for argon than for nitrogen, and that the dependence on the trap geometry scales like length^2/radius^3. In the end, it was determined that these traps will introduce an insignificant flow impedance (less than 0.1 bar) when integrated into the LZ Xenon Purification System.

CHAPTER I

Introduction

1.1 The Dark Matter Problem

There was a time at the end of the 19th century when some people thought that physics was finished: that we already knew everything fundamental about the universe, and all that remained was more precise measurements (*Horgan*, 2015). In the early 20th century, this notion was completely overturned as new concepts such as quantum theory and Einstein's relativity shook up the physical landscape. Since then, humanity has made tremendous leaps forward in fundamentally understanding the universe. For example, the discovery of the Higgs boson in 2012 and the detection of gravitational waves in 2015 were monumental discoveries in support of the Standard Model of particle physics and General Relativity, respectively (CERN, Caltech). Despite these advances, the specifics of what precisely makes up the universe has remained nebulous. As far back as the 1930s, astronomers studying the motions of stars and galaxies observed that there is more matter in the universe than meets the eye (*Bertone and Hooper*, 2016). In fact, it is estimated that the atoms and molecules that make up the world around us compose only 20% of the mass in the universe. The remaining 80% is something more exotic, and has been given the mysterious name ''dark matter''(*Garrett and Duda*, 2011).

What makes this dark matter so elusive is that we cannot directly see it – it gives off no light. Still, there is an overwhelming amount of indirect evidence that supports the existence of dark matter. In the 1970s, astronomers saw that stars orbiting on the outer edges of galaxies move much faster than expected. Elementary gravitational physics would suggest that stars further from the center of a galaxy should move slower since the gravitational force pulling on them is weaker at longer distances. However, stars far from the centers of galaxies appear to be moving much faster than expected. This implies that there is a stronger gravitational force pulling on these stars than expected, and therefore that there is more mass hidden in galaxies than astronomers can see (*Bertone and Hooper*, 2016). There is much more evidence supporting the existence of this invisible dark matter. For example, gravitational lensing of galaxies is stronger than it should be based on the amount of visible mass in the universe, and precise measurements of the Cosmic Microwave Background have revealed that there is more mass in the universe than can be accounted for by visible

matter alone (*Garrett and Duda*, 2011). Each of these instances shares the common theme that there is more mass present than what we can see.

Even with all of this evidence in support of the existence of dark matter, the exact nature of dark matter remains unknown. Nevertheless, there are some clues as to what dark matter might be composed of. Precision studies of Big Bang Nucleosynthesis and the Cosmic Microwave Background have revealed that dark matter can emphatically not be comprised of ordinary baryonic matter – the atoms and molecules that make up the world as we know it (*Freese*, 2017). Beyond this, we know that dark matter must not carry any electric charge or else it would interact with light, thereby allowing us to have seen it. Additionally, dark matter must be massive because we have witnessed its gravitational influence on galaxies. Finally, dark matter must be stable because if it were not, we would be able to detect decays of dark matter (*Garrett and Duda*, 2011). We do know of one particle on the Standard Model that meets all of these criteria: the neutrino. Unfortunately, neutrinos are unsuited to be true dark matter candidates. Not only are their masses too small, but neutrinos also move much too fast to account for the large scale structural formation of the universe (*Bertone and Hooper*, 2016). Therefore, we are forced to conclude that dark matter is something new – something beyond the Standard Model of particle physics.

1.2 WIMP Search

One theory of dark matter broadly classifies dark matter candidates as so-called Weakly Interacting Massive Particles (WIMPs). As the name suggests, these particles interact weakly with ordinary matter, making them very difficult to detect. There are three main methods for detecting WIMPs. The first is WIMP production, in which colliders such as the Large Hadron Collider aim to create dark matter particles as products of high energy particle collisions. The second is indirect detection, where telescopes search for energy signatures of dark matter particle annihilations in the galaxy. Finally, there is direct detection, whereby physicists search for WIMPs interacting directly with atomic nuclei (*Garrett and Duda*, 2011). This sort of direct detection scheme is employed by several experiments around the world, including the LUX-ZEPLIN Dark Matter Experiment (LZ).

The main idea underlying direct detection experiments like LZ is as follows. As the Earth moves through the Milky Way, the dark matter particles that fill the galaxy are continuously passing through and around the Earth. Every so often, some WIMPs interact – albeit weakly – with the ordinary baryonic matter on the planet. By setting up a large and sensitive target for a sufficiently long time, one should be capable of directly detecting these WIMP interactions. LZ uses seven tonnes of liquid xenon as its active target material, which has several advantages. Since xenon is a noble gas, it is chemically inert. It also has no long-lived radioisotopes, thereby reducing its own contribution to background signals. Additionally, xenon has a heavy nucleus, which makes it a large target for WIMPs to collide with, increasing the probability of detection (*Mount*, 2017).

1.3 The LUX-ZEPLIN Radon Removal System

WIMP interactions with ordinary matter are expected to be extremely rare; therefore, one of the major challenges faced by direct detection experiments is the discrimination of experimental backgrounds. One of the most troublesome backgrounds for LZ is radon, which poses several problems for the experiment. The most immediate threat presented by radon is that one of its decay granddaughters – ^{214}Pb – has a naked beta decay that may mimic expected WIMP signals (*Mount*, 2017). The presence of such signals severely limits the sensitivity of the detector, and so they must be removed. Unfortunately, radon is particularly problematic to eliminate: it is a noble gas, and so it cannot be removed by chemical means. Additionally, radon is continuously re-supplied to the LZ system by detector components such as feedthroughs and cables, meaning that it must be continuously filtered out of the system (*Pushkin et al.*, 2018).

In an effort to address the complications introduced by radon, the University of Michigan developed a Radon Removal System (RRS) for the LZ experiment. For two years, the University of Michigan Dark Matter Group studied the properties of charcoal in an effort to design a charcoal trap which would lower radon background rates present in the LZ detector by 90% (*Pushkin et al.*, 2018). Charcoal has been used in previous low background experiments such as XMASS (*Abe* (2012)) and SNO+ (*Golihtly* (2008)) due to its ability to trap radon atoms long enough for them to decay. The studies performed at the University of Michigan determined the optimal charcoal type and mass with which to design the LZ RRS (*Pushkin et al.*, 2018). A fully functional RRS has been constructed based on the results from these studies for the LZ Xenon Purification System (XPS).

Upon its integration into LZ, the RRS will be one of several components in the larger XPS. Consequently, it is important that the finalized RRS not introduce too large of a flow impedance to the circulation of the system at large. If the RRS provides too much impedance under normal operating conditions, additional hardware may be required to circulate the xenon. Therefore, studies of gas flow dynamics in the finalized RRS traps were required in order to ensure a successful integration into the LZ XPS. These studies are the primary focus of this thesis.

1.4 Motivation For Flow Impedance Measurements

The gas flow impedance introduced by the RRS traps will be determined by measuring the difference in pressure between the inlet and outlet of the traps at various flow rates. In order for these traps to be integrated smoothly into the LZ XPS, the pressure differential between the inlet and outlet of the traps must be small compared to the operating pressure of 1.6 bar. Therefore, the primary goal of these measurements is to demonstrate that the pressure difference between the trap inlet and outlet is much less than 0.1 bar at the LZ RRS operating flow rate (0.5 standard liters per minute (slpm)), temperature (188 K) and pressure (1.6 bar).

Preliminary gas flow impedance measurements were conducted in August 2018.

These tests did not utilize the full architecture of the RRS or precise instruments, as they were intended to give only a rough estimate of the impedance. For this reason, a new set of measurements was devised for January 2019 in order to test the trap performance in an environment more closely resembling the true LZ experimental conditions.

CHAPTER II

Methods

2.1 System and Setup

The measurements of the gas flow impedance of the LZ RRS were conducted using a combination of components from the prototype and final RRS. The gas flow panel from the prototype RRS was used to control the system pressure and the gas flow rate through the charcoal traps. Details concerning this panel can be found in (*Pushkin et al.*, 2018). Most of the circuitry of this panel was bypassed; the only components utilized from this panel were the pressure regulator and gas flow meter. A simplified flow diagram of the system used in these final flow impedance measurements can be found in Figure 2.1. The prototype RRS panel components of this circuit were made from $\frac{1}{4}$ inch ultra-high vacuum pipes and valves, however the majority of the system was constructed using $\frac{1}{4}$ inch polyethylene tubings and swagelok connections, which made for fast and flexible circuit construction. Special care was taken to limit the length of the tubing connecting the cryostat and pressure differential meters, as extended connections created a significant impedance in the connection lines.

The circuit in this experiment was operated as follows. Gas entered the prototype RRS gas panel from either a boiled-off nitrogen dewar or a research grade argon gas bottle. The gas flow rate through the system was regulated by a pressure regulator and monitored by a mass flow meter (Model:179A01314CR3AM, MKS), both from the prototype RRS gas circulation system. From here, the flow left the prototype RRS gas circulation system and was directed through the charcoal traps, which were housed in a cryostat that had previously been used for the prototype RRS (*Pushkin et al.*, 2018). After flowing through the charcoal traps, the gas was directed through a needle valve. This valve was used to control the system pressure for measurements conducted at pressures higher than atmospheric. From here, the gas was directed to an exhaust duct and vented to atmosphere.

The cryostat used for these measurements is the same cryostat that will used in the LZ RRS. The vacuum jacketed cryostat has an inner diameter (ID) of 32 cm and a height of 132 cm. It was filled with Novec-7100 engineered fluid in order to regulate the temperature of the charcoal traps inside. The cryostat could be cooled down and maintained at the LZ operating temperature of 188 K by an EK-90 refrigerator as needed. Two of the four stainless steel charcoal traps from the LZ RRS were connected

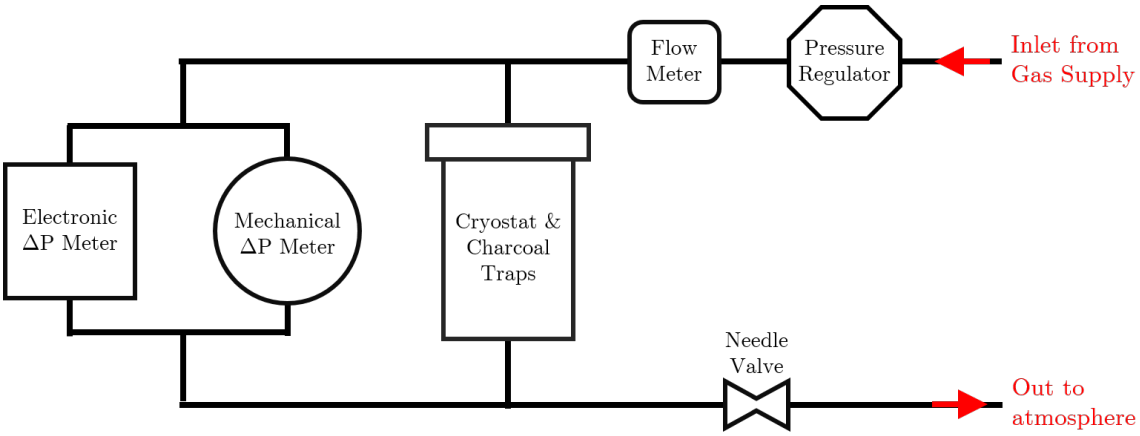

Figure 2.1: Flow diagram for the flow impedance measurements. The prototype RRS gas panel was used only for the pressure regulator and flow meter. The two ΔP meters used were connected as closely to the cryostat as possible to minimize losses to the connection line impedance. Two of the four charcoal traps from the LZ RRS were placed in the cryostat. The needle valve at the outlet of the circuit was used only to control the pressure of the system.

in series in this experiment – one "Big Trap" (10.1 cm ID x 79.4 cm height) containing 4.5 kg of Saratech charcoal (Blücher GmbH.), and one "Small Trap" (7.6 cm ID x 73.0 cm height) containing 2.2 kg of Saratech charcoal. Drawings for these traps can be found in Figure 2.2. The Saratech charcoal used in these flow measurements is the same brand of charcoal being used for the LZ RRS (*Pushkin et al.*, 2018).

To measure the flow impedance in the system, two pressure differential gauges were connected in parallel with the cryostat, one mechanical (Dwyer 2000-00AV) and one electronic (MKS Type 120AD). The majority of the data collection was performed using readings from the electronic pressure differential (ΔP) meter due to its high precision. The mechanical gauge was the same gauge used in the preliminary measurements conducted in August 2018. It was included in these measurements despite its relatively low precision compared to the electronic gauge in order to allow for cross checks with the previous measurements.

2.2 Experimental Procedure and Data Acquisition

Data acquisition began with the gas of choice (argon or nitrogen) being flushed through the entire system at 6 slpm for 30 minutes in order to drive out system impurities. After flushing the system, the flow rate was reduced to 2 slpm using the pressure regulator and left to stabilize for an hour. During this hour, the pressure differential measured by the electronic and mechanical gauges and the gas flow rate were monitored for fluctuations. If significant fluctuations in the flow rate and pressure differential readings (±10%) persisted after this stabilization period, the stabiliza-

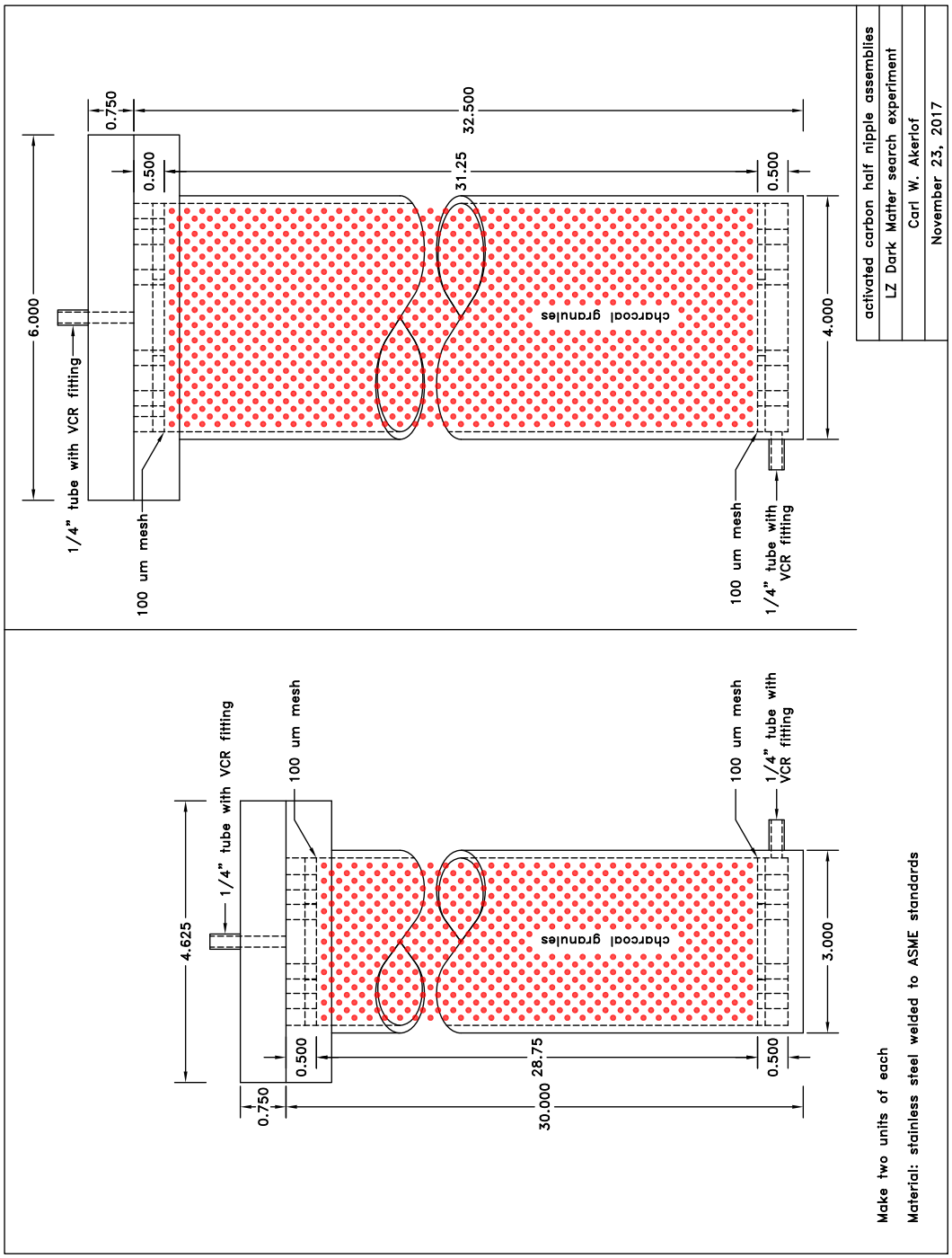

Figure 2.2: Drawings for the stainless steel traps used in the RRS. Dimensions in the drawing are in inches, as this is the LZ unit convention. The top drawing is the Small Trap; the bottom drawing is the Big Trap.

tion time was extended as needed in 30 minute increments to ensure system stability before proceeding.

Once the system flow and pressure stabilized, measurements of the trap flow impedance commenced. The time, flow rate, and ΔP readings from the electronic and mechanical gauges were recorded in 10 minute intervals three times for each set of parameters. After taking data at 2 slpm, the measurements were repeated at 1 slpm and 0.5 slpm. These sets of measurements were repeated for each combination of experimental parameters detailed in Table 3.1.

Sets of measurements were conducted at room temperature (295 K) and the LZ RRS operating temperature of 188 K. Measurements were generally conducted at atmospheric pressure (1.0 bar), with the lone exception being a set of measurements conducted with argon at 188 K and 1.6 bar – the LZ RRS operating conditions. Measurements using different trap sizes (the Small and Big Traps individually, and then both traps connected in series) were conducted outside of the cryostat assembly to avoid cumbersome cryostat deconstructions that would be required in order to change traps between measurements. For this reason, measurements using different trap sizes were only performed at room temperature and atmospheric pressure.

In addition to these primary measurements, separate trials were conducted to determine the baseline impedance introduced by the connecting hoses in each trial. These began by connecting the hoses which joined the traps to the rest of the gas circuit together. Trials were conducted using argon and nitrogen gases at 0.5, 1.0, and 2.0 slpm at 295 K and 1.0 bar. The results of these measurements were then used to remove the connection hose baseline factors from the primary trials, thereby isolating the impedance from the traps for analysis.

Finally, a set of measurements was performed using nitrogen gas at 295 K and 1.0 bar through two 60 μm particle filters connected in series at 0.5, 1.0, and 2.0 slpm. These meshes may be used in the LZ RRS as an extra precaution to prevent the possibility of dust being carried into the LZ detector volume in case the 100 μm meshes in the traps are not sufficient to do so. Since it was not known at the time of experimentation whether these filters would be used in the LZ RRS, the measurements were made separately from the combined trap trials. The measurements were intended to see whether these filters would push the total flow impedance of the system above the LZ RRS pressure differential maximum of 0.1 bar.

CHAPTER III

Analysis

3.1 Results

The combinations of parameters tested in this experiment are tabulated in Table 3.1 for reference. Three data points were taken at each set of parameters (e.g. three data points were taken with argon at 295 K and 1.0 bar through the Small Trap at 0.5 slpm). The results of these measurements can be found in Figures 3.2 and 3.1. Note that the argon data points in Figure 3.2 were taken at 0.8, 1.6, and 3.2 slpm, while the nitrogen data were taken at the nominal 0.5, 1, and 2 slpm. This factor of 1.6 discrepancy is the result of the wrong correction factor being applied to the gas flow meter during data collection. The flow rates were corrected during the analysis, resulting in the different flow rate values for argon and nitrogen trials seen in Figure 3.2. Note that where applicable, the impedance contribution from each connection hose has been subtracted from the flow impedance, with the hose impedance values tabulated in Table 3.2

Some general trends, which will be explored in the subsequent sections, can be drawn from these figures. First, the pressure differential decreases as temperature decreases, as seen in Figure 3.2. Second, the pressure differential is higher in trials using argon gas than it is in the equivalent trial using nitrogen, which can be seen when comparing the measurements in Figure 3.2. Next, the pressure differential decreases as the average system pressure increases, as can be seen by comparing the 1.0 bar and 1.6 bar data in Figure 3.2. Finally, we see that in Figure 3.1, the Small Trap introduced a higher pressure differential than the Big Trap in all cases despite containing less charcoal.

In addition to these points, there appears to be a discrepancy in Table 3.1. If we add the flow impedances from the Small and Big Traps for either nitrogen or argon, we would expect to recover the flow impedance from the corresponding Combined Trap measurements since the "Combined" Trap consists of the Small and Big Traps connected in series. However, performing this calculation, we find a difference of nearly 15% between the Combined Trap flow impedance and the sum of the Small and Big Trap flow impedances. This discrepancy appears despite the fact that the different connection hose contributions to the flow impedances have been subtracted from the data. In view of this, the extrapolations made by adding successive traps in

series can only be said to be accurate to 15%.

The fits in Figures 3.2 and 3.1 are single parameter linear regressions of the form of Equation (3.2) using least-squares fitting. The reasons for fitting to this functional form (i.e. Ohm's Law) will be discussed in the subsequent sections. The values of the fit slopes are shown in Table 3.1, denoted as Z_{flow}.

Gas	**Temperature** [K]	**Pressure** [bar]	**Trap**	$\mathbf{Z}_{flow}$ [psi/slpm]
N_2	295	1.0	Combined	0.050
N_2	295	1.0	Small	0.036
N_2	295	1.0	Big	0.020
N_2	188	1.0	Combined	0.025
N_2	295	1.0	60 μm Filters	0.29
Ar	295	1.0	Combined	0.065
Ar	295	1.0	Small	0.049
Ar	295	1.0	Big	0.027
Ar	188	1.0	Combined	0.034
Ar	188	1.6	Combined	0.022

Table 3.1: Comprehensive table of trials conducted to test gas flow through the LZ RRS traps. Three data points were taken at each combination of parameters at each flow rate (e.g. 0.5, 1.0 and 2.0 slpm). The "Combined" traps refer to the Big and Small traps connected in series within the LZ RRS cryostat. The "Big" and "Small" traps refer to the individual Big and Small trap trials taken outside the cryostat. Z_{flow} is calculated as the slope of the pressure differential plotted against flow rate, as given in Equation (3.2). Where applicable, the flow impedance contributions from the connection hoses have been subtracted from the measurements.

Gas	**Traps Used**	$\mathbf{Z}_{flow}$ [psi/slpm]
N_2	Combined	$3.7{\cdot}10^{-3}$
N_2	Big / Small	$1.5{\cdot}10^{-2}$
Ar	Combined	$4.9{\cdot}10^{-3}$
Ar	Big / Small	$1.9{\cdot}10^{-2}$

Table 3.2: Table of connection hose impedance measurements. Three data points were taken at each flow rate (i.e. 0.5, 1.0 and 2.0 slpm). The impedance is larger for the "Big / Small" trials because longer connection hoses were needed to join the pressure differential meter to the traps in these measurements.

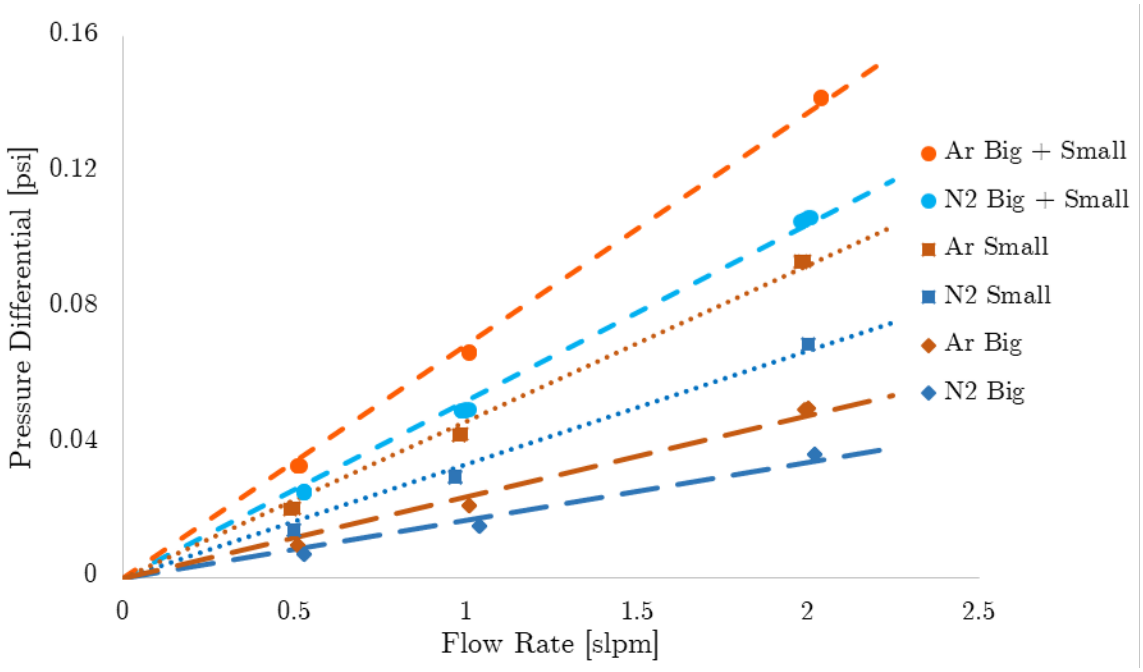

Figure 3.1: Pressure differential plotted as a function of gas flow rate. Measurements were conducted at 295 K, 1.0 bar, and with both nitrogen and argon gases. Here, the Small and Big Traps were tested both individually and while connected in series (Big + Small). Here, the flow impedance contributions from the connection hoses have been subtracted from the measurements.

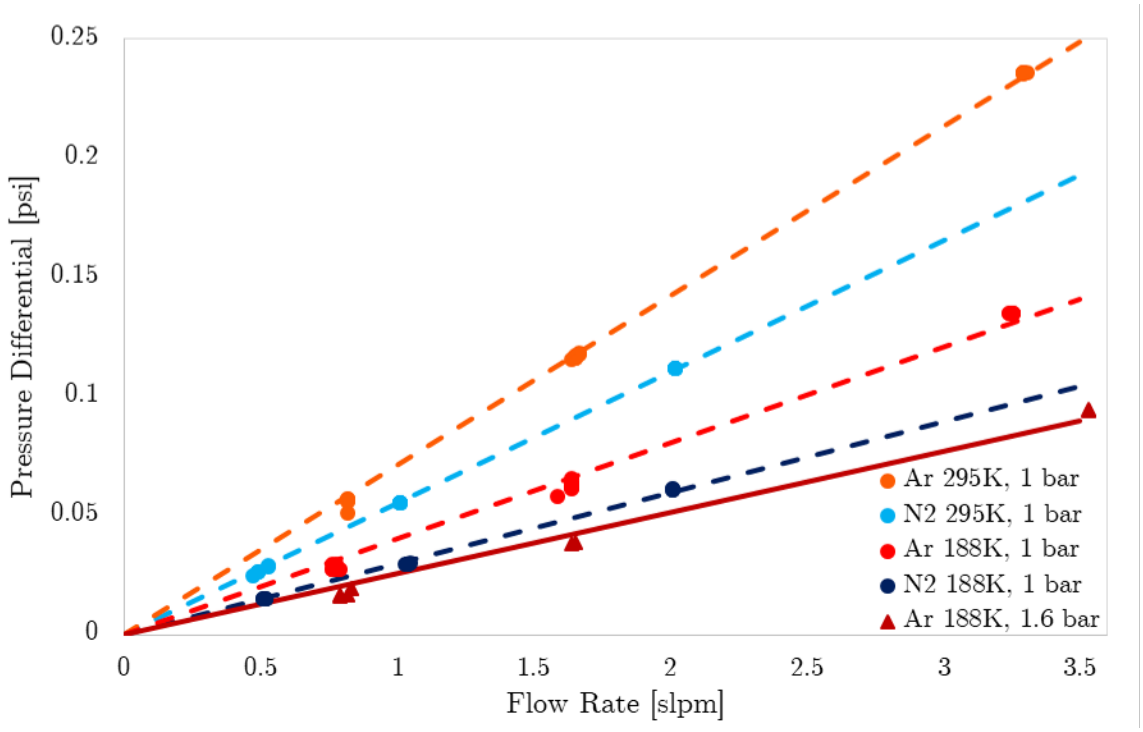

Figure 3.2: Pressure differential plotted as a function of gas flow rate. Measurements were conducted at both 295 K and 188 K, and at 1.0 bar for both argon and nitrogen gases, with an additional measurement made at 1.6 bar with argon at 188 K. All measurements were made with the Big and Small traps connected in series. Here, the flow impedance contributions from the connection hoses have been subtracted from the measurements.

3.2 Fluid Dynamics in the LZ Radon Removal System

In order to extract insightful information from these results, it is important to understand the fluid dynamics governing the system.

3.2.1 Viscous Flow

Generically, there are two broad categories of fluid flow: viscous flow and molecular flow. Viscous flow is characterized by the fluid interacting with itself more strongly than with its container (most everyday fluids such as water from a faucet operate under such conditions). Molecular flow has the opposite characterization: the fluid will tend to interact more with its container than with itself (this is generally the case for vacuum systems). Whether a system operates under viscous or molecular flow is determined by the Knudsen number K,

$$K = D/\lambda, \tag{3.1}$$

which is a dimensionless parameter defined as the ratio of the diameter D of the channel through which a fluid flows to the mean free path λ of molecules in the fluid. If this number is greater than 110, the flow is viscous; if the number is less than 1, the flow is molecular (*Roth*, 1982). In the case of this experiment, a typical Knudsen number can be calculated based on the methods outlined in (*Roth*, 1982) to be on the order of 2000 which, according to Roth, we can treat as viscous flow.

Viscous gas flow can be modeled by Ohm's Law for fluids as

$$\Delta \mathrm{P} = QZ_{flow}. \tag{3.2}$$

Here, ΔP is the pressure difference between the inlet and outlet of the system (analogous to the voltage on an electrical circuit), Q is the volumetric flow (analogous to electrical current), and Z_{flow} is the gas flow impedance. The flow impedance can be broken down into further constituents characteristic of the system through which the gas flows, and will be discussed in Section 3.2.3. An important feature of this equation is the linear scaling of ΔP with the gas flow rate. This feature is retained for a special class of viscous flow – laminar flow – while the scaling becomes nonlinear as the flow becomes more turbulent (*Roth*, 1982).

3.2.2 Laminar and Turbulent Flow

As mentioned in the Section 3.2.1, there are two major subsets of viscous flow: laminar and turbulent. Laminar flow is smooth and uniform, as shown in Figure 3.3, while turbulent flow is rough and disorderly, as shown in Figure 3.4. Turbulent flow is typical of fluids which are flowing very quickly through tight channels, causing the fluid to interact with itself too strongly to maintain a peaceful flow. An important consequence flow being turbulent rather than laminar is that turbulent flow will encounter higher flow impedance than laminar flow due to its non-uniform nature. This means that instead of the pressure differential varying linearly with the volumetric flow rate as it does in Ohm's Law, the pressure differential will scale at some higher

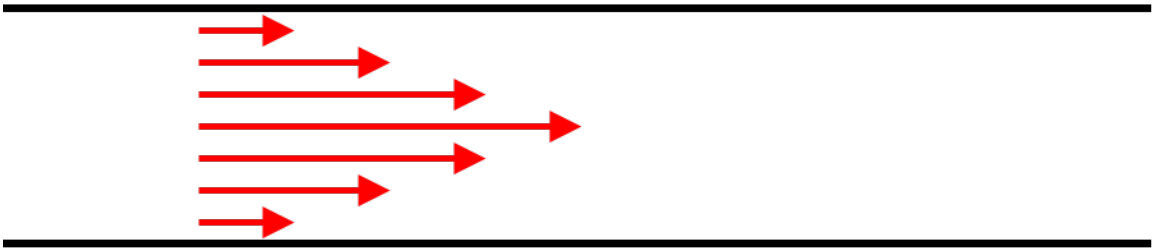

Figure 3.3: Cartoon of laminar fluid flow. Characterized by smooth, straight flow lines that are fastest at the center of the channel.

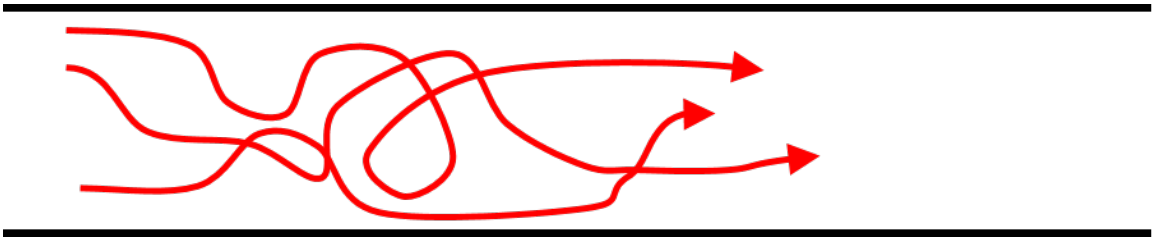

Figure 3.4: Cartoon of urbulent fluid flow. Characterized by chaotic flow lines.

power of the flow rate. This is because the impedance in the system will rise as the flow becomes more turbulent instead of remaining constant as it does in laminar flow (*Roth*, 1982).

To determine which of these flow classes the gases in this experiment operated under, we must consult the Reynold's number of the system. The Reynold's number R_e is defined as

$$R_e = \frac{\rho v D}{\eta}. \tag{3.3}$$

Here, ρ is the density of the gas, v is the linear velocity, D is the diameter of the aperture through which the gas flows, and η is the viscosity. A Reynold's number less than 1100 is characteristic of laminar flow, numbers greater than 2100 are characteristic of turbulent flow, and there is a transition region in between (*Roth*, 1982).

In order to compute the Reynold's number, some conversions are required. While the viscosity and aperture diameter can be determined directly from the system, the density and velocity require more work to extract from our system. The gas density can be extracted using the ideal gas law, given by

$$PV = nRT = \frac{mRT}{M}. \tag{3.4}$$

Here, P is the gas pressure, V is the volume, n is the number of moles of gas in the system, R is the ideal gas constant, T is the gas temperature, m is the total mass of a gas in use, and M is the molar mass of the gas. Solving this equation, we can

derive the gas density as

$$\rho = \frac{m}{V} = \frac{PM}{RT}. \tag{3.5}$$

Thus, we have expressed the gas density in terms of constants and known system parameters.

Next, the linear velocity v of the gas can be rewritten using the definition of volumetric flow as

$$v = \frac{Q}{A}, \tag{3.6}$$

where A is the cross sectional area of the flow channel. Again, we have expressed an unknown in terms of known system parameters.

Combining these derived parameters, the Reynold's number becomes

$$R_e = \frac{PMQD}{RTA\eta}. \tag{3.7}$$

Now we are almost ready to calculate the Reynold's numbers for the experiment. One set of parameters remains to be determined: the characteristic diameter D and cross sectional area A of the flow channels. Naively, one could use the dimensions from the charcoal cylinders here and move on; however this ignores the presence of the charcoal within these cylinders altogether. Instead, we must analyze the small gaps between individual pellets of charcoal.

As shown in (*Pushkin et al.*, 2018), Saratech granules are nearly spherical in shape, with diameters on the order of 0.05cm. If we assume a uniform packing, gaps between Saratech granules will be arranged as in Figure 3.5. This sort of packing would lead to gaps between the granules on the order of one fifth of the size of the granules themselves. Under this approximation, the characteristic diameter D is roughly 10^{-4} m and the cross sectional area A is roughly $3 \cdot 10^{-8}$ m^2. Substituting these into Equation (3.7), we can finally compute our Reynold's numbers for the system.

Using Equation (3.7), the Reynold's numbers characteristic of these measurements fall between 4000 and 50,000. Since the turbulent flow regime is marked by Reynold's numbers greater than 2100, we can say that gas flowing through our system is generally turbulent. This makes sense based on what is seen in the data in the Section 3.1. Looking closely, the data seem to exhibit varying degrees of nonlinear behavior. For example, plots with nitrogen at room temperature (which have the lowest Reynold's numbers) appear to be nearly linear, however the plots using argon at 188 K (which have the highest Reynold's numbers) appear to deviate from the linear fits in some higher-order manner, although the exact manner cannot be determined from the current analysis. Thus, we can see that the measured pressure differentials seem to be influenced by the flow turbulence, which is correlated to the Reynold's number.

In the grand scheme, the data sets in the Section 3.1 do not appear to deviate too extremely from being linear. One might imagine that at higher flow rates, the perceived nonlinearity of the pressure differentials would become more apparent. At the flow rates used in these measurements however, the nonlinear behavior of the data, if any, is fairly small. For this reason, Ohm's Law for fluids will still be applied

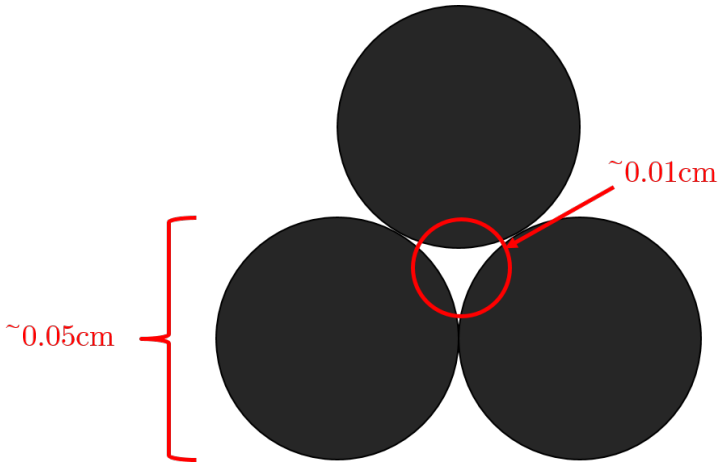

Figure 3.5: Schematic of individual Saratech sphere packing. It is assumed that this sort of arrangement is how all of the Saratech pellets pack in the charcoal columns.

to the analysis of these results, though it will be important to keep the truly turbulent nature of the flow in mind in the subsequent analysis.

3.2.3 Ohm's Law for Fluids

Because we will be approximating our system as being described by Ohm's Law, we will expand upon our discussion of Equation (3.2). To understand how changing the experimental parameters (temperature, gas species, etc.) should affect the measured pressure differentials, it is instructive to expand the flow impedance in this equation. When expanding the impedance out into all of its constituents as shown in (*Roth*, 1982), Ohm's Law can be rewritten as

$$\Delta \mathrm{P} = QZ_{flow} = Q\left(\frac{16}{\pi^{5/2}}\right)\left(\frac{L}{r^4}\right)\left(\frac{1}{\bar{P}}\right)\left(\frac{\sqrt{m}}{a^2}\right)\left(\frac{\sqrt{k_B T^3}}{T+C}\right), \tag{3.8}$$

where the flow impedance has been expanded into all of its constituent dependencies. Each grouping of the terms corresponds to each of the experimental parameters being tested. The first term is a constant. The second represents the dependence on the geometry of the fluid channel, with L being the length of the channel and r being the channel radius. Next is the dependence on the average system pressure $\bar{P}$. Following this is the ΔP dependence on the gas species being used: m is the mass of each gas molecule and a is the molecular radius. The final term represents the dependence on temperature T, with the so-called Sutherland's constant C, which is characteristic of the gas being used, and Boltzmann's constant k_B (*Roth*, 1982).

Because this version of Ohm's Law is large and complicated, it would be useful to isolate each of these embedded dependencies for independent study. Fortunately, it is possible to decouple most of the the individual dependencies. By holding all but one set of parameters constant, a single dependence can be extracted by taking the ratio of Z_{flow} for one parameter to another parameter. This can be accomplished

by making two measurements, for example one with nitrogen at 295 K and 1.0 bar through the Big Trap, and another with the same parameters but at 188 K. After taking these measurements, we can divide the measured flow impedance values to effectively isolate the temperature dependence from Equation (3.8) in a ratio as this example indicates

$$\frac{Z_{295\ K}}{Z_{188\ K}} = \frac{\sqrt{T^3_{295\ K}}}{(T_{295\ K} + C_{N_2})} \frac{(T_{188\ K} + C_{N_2})}{\sqrt{T^3_{188\ K}}}. \tag{3.9}$$

Since all parameters besides the temperature are held constant between the measurements, everything except the temperature dependence cancels out in the division, allowing us to isolate one parameter set at a time. In this way, comparing measurements made with all but one parameter being held constant allows each of the dependencies in Ohm's Law to be evaluated individually.

The individual dependencies in Ohm's Law can be isolated into ratios for all sets of parameters from this experiment using this method. The following are the isolated dependence ratios tested in this experiment, along with the computed theoretical values for each ratio.

Average Pressure

$$\frac{Z_{1.0\text{ bar}}}{Z_{1.6\text{ bar}}} = \frac{\bar{P}_{1.6\text{ bar}}}{\bar{P}_{1.0\text{ bar}}} = 1.6 \tag{3.10}$$

Gas Species

$$\frac{Z_{\mathrm{Ar}}}{Z_{\mathrm{N_2}}} = \frac{\sqrt{m_{\mathrm{Ar}}}}{a^2_{\mathrm{Ar}}} \frac{a^2_{\mathrm{N_2}}}{\sqrt{m_{\mathrm{N_2}}}} \frac{(C_{\mathrm{N_2}} + T_{188\ K,\ 295\ K})}{(C_{\mathrm{Ar}} + T_{188\ K,\ 295\ K})} \approx 1.1\ (188\text{ K}),\ 1.1\ (295\text{ K}) \tag{3.11}$$

Temperature

$$\frac{Z_{295\text{ K}}}{Z_{188\text{ K}}} = \frac{\sqrt{T^3_{295\ K}}}{(T_{295\ K} + C_{Ar,N_2})} \frac{(T_{188\ K} + C_{Ar,N_2})}{\sqrt{T^3_{188\ K}}} \approx 1.5\ (\mathrm{Ar}),\ 1.4\ (\mathrm{N_2}) \tag{3.12}$$

Note that the gas species and temperature dependencies remain coupled after taking the ratios. This is due to the presence of Sutherland's constant in the temperature term, which is characteristic of each gas being used.

Channel Geometry

$$\frac{Z_{Small}}{Z_{Big}} = \frac{L_{Small}}{r^4_{Small}} \frac{r^4_{Big}}{L_{Big}} \approx 2.9 \tag{3.13}$$

This would be the case if the traps were empty tubes; however, the presence of the charcoal complicates things. Drawing on Figure 3.5, the actual channel parameters should be $L = 5 \cdot 10^{-4}$ m and $r = 5 \cdot 10^{-5}$ m. If we assume a uniform packing of the charcoal in the traps, we can model the charcoal bulk as as stack of uniform disks of charcoal. In this model, the channels through each disk would be connected in parallel, with the number scaling with the area of a disk, and the number of disks connected in series would scale with the length of the trap. If we account for this, then Equation (3.13) becomes:

$$\frac{Z_{Small}}{Z_{Big}} = \frac{L_{channel}}{r^4_{channel}} \frac{r^4_{channel}}{L_{channel}} \frac{N_{\text{series, Small}}}{N_{\text{parallel, Small}}} \frac{N_{\text{parallel, Big}}}{N_{\text{series, Big}}} = \frac{L_{Small}}{r^2_{Sm2ll}} \frac{r^2_{Big}}{L_{Big}} \approx 1.6 \qquad (3.14)$$

3.3 Evaluating Observed Flow Impedance Dependencies

The isolated parameter dependence ratios from Section 3.2 are consolidated in Table 3.3 for reference.

Parameter Ratio	Model Ratio	Data Ratio
$Z_{295\ K}/Z_{188\ K}$	1.5 (Ar), 1.4 (N_2)	1.95 (Ar), 2.05 (N_2)
$Z_{1.6\ bar}/Z_{1\ bar}$	1.6	1.56
$Z_{\text{Ar}}/Z_{\text{N}_2}$	1.1 (295 K & 188 K)	1.27 (295 K), 1.30 (188 K)
$Z_{\text{Small}}/Z_{\text{Big}}$	1.6	1.92 (Ar), 1.96 (N_2)

Table 3.3: Comparison of the model calculated and data calculated parameter dependence ratios.

When comparing these observed dependencies in Table 3.3, we see many disagreements between the data and the Ohm's Law model. In fact, only the system pressure dependence appears to be consistent between the data and the model. The most likely cause for these discrepancies is the fact that we approximated our system as being described by Ohm's Law, which is generally applied to laminar flow systems while we know from Section 3.2.2 that our system flows were more turbulent in nature. Let us now go through each dependence individually to address the differences one by one.

3.3.1 Pressure

The Z_{flow} ratios for measurements at different system pressures are fairly consistent between the model and the data (the model predicts $Z_{1.6\ bar}/Z_{1\ bar} = 1.6$, and the data yields $Z_{1.6\ bar}/Z_{1\ bar} = 1.56$). This suggests that the average system pressure has an equivalent effect on the flow impedance in both laminar and turbulent flow systems. This correspondence makes sense when considering that pressure is an intensive feature of the gas, and does not have much bearing on interactions with the charcoal environment, as seen in (*Pushkin et al.*, 2018). It is possible that this correlation might not hold for the xenon gas in the LZ system since xenon will tend to adsorb more onto charcoal at increasing pressures (*Pushkin et al.*, 2018). Therefore, though not seen here, the adsorption of xenon on charcoal may complicate the impact that the system pressure has on flow impedance in the LZ RRS.

3.3.2 Temperature

The measured Z_{flow} ratios for different system temperatures were significantly different from the model values. One interesting difference between the model and data is the fact that while in the model, argon has a slightly stronger temperature

dependence than nitrogen ($Z_{295\ K}/Z_{188\ K} = 1.5$ for Ar and 1.4 for N_2), the data shows the opposite trend ($Z_{295\ K}/Z_{188\ K} = 1.95$ for Ar, 2.05 for N_2). These discrepancies between the model and data are likely attributable to turbulent flow in the system.

As discussed previously, the flow in our system is not actually laminar despite our use of Ohm's Law to model the system. Due to the chaotic nature of turbulent flow, it is likely that lower temperatures reduce the amount of turbulence in the system due to there being a lower average kinetic energy for the gas. In this way, additional effects from turbulent impedance should be smaller at low temperatures than they are at high temperatures. This would lead to the observed behavior where the flow impedance ratio between the 295 K and 188 K measurements is larger than it is in the Ohm's Law model.

Regarding the nitrogen and argon discrepancy, it is possible that the diatomic makeup of nitrogen causes its turbulence to be more extreme than for monatomic argon. Under this assumption, the self-interactions of diatomic gases may have a stronger temperature dependence than monatomic atoms. This would lead to the observed correlation that the flow impedance depends more strongly on temperature in nitrogen than in argon. There is also the possibility that some systematic error is responsible for the observed difference. It is unclear how this behavior would extend to xenon gas, as xenon is known to adsorb onto charcoal in large quantities at lower temperatures (*Pushkin et al.*, 2018). In any case, this requires further study.

3.3.3 Gas Species

As seen in Equation (3.11), Ohm's Law does not predict much of a difference between argon and nitrogen gases ($Z_{\mathrm{Ar}}/Z_{\mathrm{N_2}} = 1.1$ for 295 K and 188 K). By contrast, the data shows that while there still does not appear to be a significant difference between the ratios at 295 K and 188 K (as seen in Equation (3.11)), there is a significant disparity in flow impedance between argon and nitrogen measurements ($Z_{\mathrm{Ar}}/Z_{\mathrm{N_2}} = 1.27$ for 295 K and 1.30 for 188 K). The precise cause for this discrepancy between the model and data for the gas species dependence is not known. One possibility is that nitrogen interacts differently with the charcoal than argon does, leading to a higher flow impedance for argon than for nitrogen. Another possibility is that the additional flow impedance from turbulence is stronger for argon than it is for nitrogen, thus leading to a higher flow impedance than expected for argon relative to nitrogen. As with the temperature analysis, it is unclear how the flow impedance would change when using xenon gas. Consequently, this species dependence requires further study to be truly understood.

3.3.4 Channel Geometry

The dependence on the channel geometry is $Z_{\mathrm{Small}}/Z_{\mathrm{Big}} = 1.6$ for the model. This ratio was calculated to be 1.96 for nitrogen and 1.92 for argon in the data, which is a significant difference in both cases. The origin of this discrepancy initially appears nebulous. Turbulent effects in the channels should be the same in both the Small and Big Traps since the gaps between charcoal granules are the same on average, so this

cannot explain the observed difference. If we consider the possibility of edge effects in the traps, however, the origin becomes a bit more clear.

The gaps between the charcoal granules and the column walls should be larger than the gaps between granules since the spherical granules are able to pack more tightly together than they would against the relatively flat trap wall. The number of such larger channels would scale with the trap circumference (i.e. proportional to r) in parallel, and with the trap length in series. Under this approximation, $Z_{\mathrm{Small}}/Z_{\mathrm{Big}}$ becomes

$$Z_{\mathrm{Small}}/Z_{\mathrm{Big}} = \frac{L_{Small}}{r_{Small}^2}\frac{r_{Big}^2}{L_{Big}}\frac{L_{\mathrm{Small}}}{r_{\mathrm{Small}}}\frac{r_{\mathrm{Big}}}{L_{\mathrm{Big}}} \approx 2.0, \tag{3.15}$$

which approximately gives the dependence observed in the data. Thus, it is likely that edge channels in the charcoal traps are responsible for the observed difference in flow impedance between the Small Trap and Big Trap.

3.4 Extrapolations for the LZ Radon Removal System

Using observations from Section 3.3, we would like to be able to make an extrapolation of the pressure drop introduced by the LZ RRS under operating conditions. The LZ RRS will have four charcoal traps (2 Small, 2 Big), making it twice the scale of the system used in these measurements. The real LZ RRS will be operated at 0.5 slpm, at 188 K, and at 1.6 bar. Therefore, using the argon pressure differential at 0.5 slpm, 188 K and 1.6 bar of roughly $7 \cdot 10^{-4}$ bar as a starting point, we can make an approximate extrapolation to the operational LZ RRS as follows.

First, we extrapolate based on the quantity of traps since two of each trap will be used in the LZ RRS instead of one. As shown in the "Small", "Big" and "Combined" data in Table 3.1, the impedance each trap introduces adds linearly to about 15% accuracy. Therefore, when extrapolating, we will double the flow impedance and add an extra 15% to account for the uncertainty from adding the traps in series. Next, computing the species dependence using Equation (3.11), $Z_{\mathrm{Xe}}/Z_{\mathrm{Ar}} \approx 0.85$, meaning that the flow impedance should actually be less for xenon than it is for argon. Despite this, there is much that is unknown about how the flow impedance will differ from these results when using xenon due to its unique adsorption properties on charcoal as seen in (*Pushkin et al.*, 2018). Consequently, we will opt to approximate xenon as having twice the flow impedance introduced by argon. This will provide a safety cushion in our extrapolated estimate for the LZ RRS.

Using these approximations, the flow impedance introduced by the LZ RRS with xenon at 0.5 slpm, 188 K and 1.6 bar would be roughly 4.6 times as much as the corresponding argon data point (two times for the trap scaling, +15% due to scaling uncertainty, two times for the argon to xenon difference). Therefore, we can extrapolate that the LZ RRS will introduce approximately $2.9 \cdot 10^{-3}$ bar of flow impedance to the LZ XPS. This is well below the goal threshold of 0.1 bar.

Beyond the contribution from the traps themselves, the prospective addition of the 60 μm particle filters would add further flow impedance to the system. The impedance denoted in Table 3.1 is based only on nitrogen gas at 295 K and 1.0 bar,

and uses two of the filters. In the LZ RRS, the system will have only one of these filters, and will operate at 1.6 bar and 188 K. Applying the temperature, pressure, and gas species dependencies from Section 3.3, we extrapolate that the impedance introduced by the single particle filter will be roughly $8.7 \cdot 10^{-3}$ bar, for a total system impedance of roughly $1.2 \cdot 10^{-2}$ bar.

Even with our added safety cushion in the argon to xenon extrapolation and the addition of the particle filter, the LZ RRS impedance is well below the goal threshold of 0.1 bar. Therefore, we expect that the LZ RRS will not cause circulation impedance problems for the XPS upon its integration.

CHAPTER IV

Conclusions

Although not all of the parameter dependencies analyzed in this experiment can be described by the Ohm's law model for laminar fluid flow, there is still merit to the modelling performed in this study. Based on the pressure and channel geometry analyses, it can be asserted that the flow impedance dependence on these parameters scales equally in both laminar and turbulent flow regimes. The temperature and gas species dependencies however appear to be more sensitive to turbulent flow, as they diverge from their Ohm's law modelling.

Of course, further study could reveal a more complete model for all of these parameters. For instance, it could be of interest to measure these dependencies at higher flow rates (i.e. at more turbulent flow) to see if this divergent behavior becomes stronger. On the opposite side of the coin, one could attempt to re-examine the dependencies at lower flow rates (i.e. towards more laminar flow) to more accurately explore the Ohm's law modelling. Beyond this, conclusive studies could be carried out using xenon gas, thereby avoiding the need to extrapolate.

Despite further work being needed to accurately describe the turbulent fluid flow, the fact that the RRS should meet the impedance threshold in the LZ XPS can be concluded from this study. Even with the padding added to the full xenon extrapolation and the additional particle filter, the potential flow impedance of $1.2 \cdot 10^{-2}$ bar introduced by the RRS should still be at least an order of magnitude below the 0.1 bar maximum for the LZ XPS. When combined with fact that no trap backup occurred during a 24 hour continuous flow study through these traps, we should expect no trouble with flow impedance when adding the RRS to the LZ XPS.

BIBLIOGRAPHY

BIBLIOGRAPHY

Abe, A. (2012), Radon removal from gaseous xenon with activated charcoal, *Nuclear Instruments and Methods in Physics Research*, *661*, 5057.

Bertone, G., and D. Hooper (2016), A history of dark matter, *Rev. Mod. Phys.*, *90*, doi:10.1103/RevModPhys.90.045002.

Caltech (2019), What are gravitational waves?, https://www.ligo.caltech.edu/page/what-are-gw.

CERN (2019), The higgs boson, https://home.cern/science/physics/higgs-boson.

Freese, K. (2017), Status of dark matter in the universe, *The Fourteenth Marcel Grossmann Meeting*, doi:10.1142/9789813226609$_0$018.

Garrett, K., and G. Duda (2011), Dark matter: A primer, *Advances in Astronomy*, *2011*, 122, doi:10.1155/2011/968283.

Golihtly, J. (2008), Characterization of a carbon radon filter and radon detection, *Master's Thesis, Queen's University*, p. 1108.

Horgan, J. (2015), *The end of science: facing the limits of knowledge in the twilight of the scientific age*, Basic Books.

Mount, B. J. (2017), Lux-zeplin (lz) technical design report, doi:10.2172/1365579.

Pushkin, K., et al. (2018), Study of radon reduction in gases for rare event search experiments, *Nuclear Instruments and Methods in Physics Research*, *903*, 267276, doi:10.1016/j.nima.2018.06.076.

Roth, A. (1982), *Vacuum Technology*, 2 ed., North Holland Publishing Co.